Towards an error indicator-based h-adaptive refinement scheme in kinematic upper-bound limit analysis with the presence of seepage forces

Xiangcou Zheng[a,b], Feng Yang[a,*], Shuying Wang[a], Junsheng Yang[a], Ashraf Osman[b]

[a] *School of Civil Engineering, Central South University, Changsha, Hunan 410075, China*
[b] *Department of Engineering, University of Durham, South Road, DH1 3LE, United Kingdom*

Abstract

This paper presents a new computational strategy for kinematic upper bound limit analysis in the presence of seepage forces with an improved mesh refinement scheme. In particular, the original adaptive refinement scheme is enhanced with a simple but efficient error-indicator of the nodal plastic dissipation for high-order elements. Adhering to the two-dimensional steady state seepage condition, numerical details regarding the calculation of total water head distributions for the seepage field are provided. In a similar manner as treating the unit weight of the soil, the effects of seepage forces are incorporated as body forces in the upper bound formulation. Numerical procedure of the proposed error indicator-based h-adaptive refinement scheme incorporating with the inclusion of seepage forces are addressed and implemented in the in-house code. Two benchmark problems are numerically analyzed to evaluate the excellent performance of the error indicator-based h-adaptive refinement scheme in kinematic upper-bound limit analysis with the presence of seepage forces.

Keywords: Error indicator; h-adaptive refinement; high order element; seepage force; upper bound limit analysis

1. Introduction

In the field of geotechnical engineering, the finite element limit analysis (FELA), which combines the plastic limit theorem with the finite element method (FEM), has been proven to be a robust approach for assessing the stability of geotechnical structures, such as soil slopes, retaining walls, foundations, tunnels, and so on. Since originally proposed by Sloan (1988, 1989) and Sloan and Kleeman (1995), both upper bound finite element method (UBFEM) and lower bound finite element method (LBFEM) have been received significant attention in the simulation of geotechnical problems (Andersen et al., 1998, 2000; Lyamin and Sloan, 2002; Krabbenhoft and Damkilde, 2003; Tin-Loi and Ngo, 2003; Krabbenhøft et al., 2007; Makrodimopoulos and Martin, 2007; Martin, 2011; Sloan, 2013; Qian et al., 2015; Yang et al., 2016, 2017; Lim et al., 2017; Xiao et al., 2018; Zhang et al., 2019b; Ukritchon and Keawsawasvong, 2018, 2019, 2020a,b; Ukritchon et al., 2020; Graine et al., 2021; Keawsawasvong and Ukritchon, 2019, 2021, 2022).

*Corresponding author
Email addresses: xczheng@csu.edu.cn (Xiangcou Zheng), yf5754@csu.edu.cn (Feng Yang), sywang@csu.edu.cn (Shuying Wang), jsyang@csu.edu.cn (Junsheng Yang), ashraf.osman@durham.ac.uk (Ashraf Osman)

In particular, the UBFEM has received extensive development due to its convenience in dealing with kinematically admissible velocity fields.

Among the existed studies using the UBFEM, the low-order finite element is usually adopted owing to its simplicity and convenience in numerical implementation as well as computational efficiency. Unfortunately, when using low-order finite elements in the framework of the UBFEM, this element can somehow lead to an over-stiff behavior especially for the area with high plastic dissipation and further result in a reduced computational accuracy (Makrodimopoulos and Martin, 2007). To address these issues, high order elements are thus introduced in the UBFEM, which has been proved to provide more rigorous solutions and preferred in this study (Sloan and Kleeman, 1995; Lyamin and Sloan, 2002; Pastor et al., 2003; Krabbenhoft et al., 2005).

As an alternative way to improve the computational performance of the UBFEM is through adaptive mesh refinement, which becomes quite promising due to its capacity in capturing intense plastic deformation zones and speeding up the numerical convergence (Makrodimopoulos and Martin, 2007; Nguyen-Xuan et al., 2016; Zhang et al., 2018). When performing an adaptive mesh refinement in the UBFEM, the fundamental thing is to determine which elements need to be refined. To control successive adaptive mesh refinement, a robust and efficient refinement indicator requires to be defined. However, in the limit analysis, the determination of a robust *priori* error estimator that governing the extent of mesh refinement is found to be quite challenging (Borges et al., 2001). Conversely, a *posterior* estimator is commonly used to predict discretization errors and thus control the mesh refinement. In this respect, various local and global indicators based on *a posterior* error estimate have therefore been proposed in some previous studies (Borges et al., 2001; Ciria et al., 2008; Munoz et al., 2009; Le, 2013; Nguyen-Xuan et al., 2016; Zhang et al., 2018). Each of these indicators has its unique set of advantages and limitations. Among these indicators, the most commonly used technique is to determine a minimal set of active element that needs to be refined through a prescribed adaptive refining coefficient (Dörfler, 1996; Martin, 2009; Nguyen-Xuan et al., 2016; Zhang et al., 2019a; Zheng and Yang, 2022). Recently, Dezfooli et al. (2022) proposed a simple error indicator along with an *h*-refinement strategy. To achieve a fully automatic adaptive analysis, a novel termination criterion ensure that the mesh refinement automatically stops is thus proposed. Unlike previous adopted mesh refinement scheme (Nguyen-Xuan et al., 2016; Zhang et al., 2019a; Zheng and Yang, 2022) with a continuously significant growth in the refined elements, the later refinement criteria ensures that the total number of refined elements gradually increases initially and then continues to decrease with adaptive step. For this reason, the error indicator and refinement criteria proposed by Dezfooli et al. (2022) are also preferred in this study and thus incorporated into the UBFEM.

It should be mentioned that, in water-rich area, the seepage effect of the groundwater is a prominent adverse factor that affects stability of geotechnical problems, and many serious engineering issuess are found to be related to the presence of seepage forces. Therefore, it is of great significance to take the influence of groundwater seepage force into consideration, as is more consistent with the actual situation (Kim et al., 1999; Chen et al., 2004; Sahoo and Kumar, 2019; Wang et al., 2021; Di et al., 2022, 2023). Within the framework of the kinematic upper bound limit analysis, in this study, a new computational strategy in the presence of seepage forces with an improved mesh refinement scheme is proposed. In particular, the original adaptive refinement scheme is enhanced with a simple but efficient error-indicator of the nodal plastic dissipation for high-order elements. Adhering to the two-dimensional steady state seepage condition, numerical details regarding the calculation of total water head distributions for the seepage field are provided. In a similar manner as treating the unit weight of the soil, the effects of seepage forces are incorporated as body forces in the upper bound formulation. Numerical procedure of the proposed error indicator-based *h*-adaptive refinement scheme incorporating with the inclusion of seepage forces are addressed and implemented in the in-house code. Two benchmark problems are numerically analyzed to evaluate the excellent performance of the error indicator-based *h*-adaptive refinement scheme in kinematic upper-bound limit analysis with the presence of seepage forces.

The content of the paper is organised as follows. After describing fundamentals of the UBFEM formulation with second-order cone programming (Section 2), Section 3 presents details and numerical implementation of the proposed error indicator-based *h*-adaptive refinement scheme in the UBFEM. Two verification examples and further discussions are finally given in Section 4.

2. Upper bound limit analysis with second-order cone programming

This section firstly presents some fundamentals of the upper bound finite element method (UBFEM) using six-node triangular elements and the governing equations for the kinematic upper bound limit analysis. Following the two-dimensional steady state seepage condition, numerical details regarding the calculation of total water head distributions for the seepage field and the formulation of second-order cone programming are thus discussed.

2.1. six-node quadratic triangular elements

For an arbitrary six-node quadratic triangular element, the horizontal and vertical velocities (u and v) within the element are assumed to be a quadratic function of the coordinates, which can be expressed as:

$$u(\boldsymbol{x}) = \sum_{i=1}^{6} N_i(\boldsymbol{x})\, u_i, \quad v(\boldsymbol{x}) = \sum_{i=1}^{6} N_i(\boldsymbol{x})\, v_i \tag{1}$$

where u_i and v_i are the horizontal and vertical velocities at node i (as shown in Fig. 1a), and $N_i(\boldsymbol{x})$ is the shape function at node i. Note that the shape function $N_i(\boldsymbol{x})$ can be expressed using area coordinates of three vertices and written as:

$$\begin{cases} N_1(\boldsymbol{x}) = L_1(\boldsymbol{x})(2L_1(\boldsymbol{x}) - 1)\,; N_4(\boldsymbol{x}) = 4L_1(\boldsymbol{x})\, L_2(\boldsymbol{x}) \\ N_2(\boldsymbol{x}) = L_2(\boldsymbol{x})(2L_2(\boldsymbol{x}) - 1)\,; N_5(\boldsymbol{x}) = 4L_2(\boldsymbol{x})\, L_3(\boldsymbol{x}) \\ N_3(\boldsymbol{x}) = L_3(\boldsymbol{x})(2L_3(\boldsymbol{x}) - 1)\,; N_6(\boldsymbol{x}) = 4L_3(\boldsymbol{x})\, L_1(\boldsymbol{x}) \end{cases}$$

in which $L_i(\boldsymbol{x}) = A_i/A$ ($i = 1, 2$, and 3), and $A = \sum_{i=1}^{3} A_i$. The definition of A_i is given in Fig. 1b. Considering a linear variation in the rates of plastic strain ($\dot{\varepsilon}$) and plastic multiplier ($\dot{\lambda}$), the values of $\dot{\varepsilon}$ and $\dot{\lambda}$ within an arbitrary finite

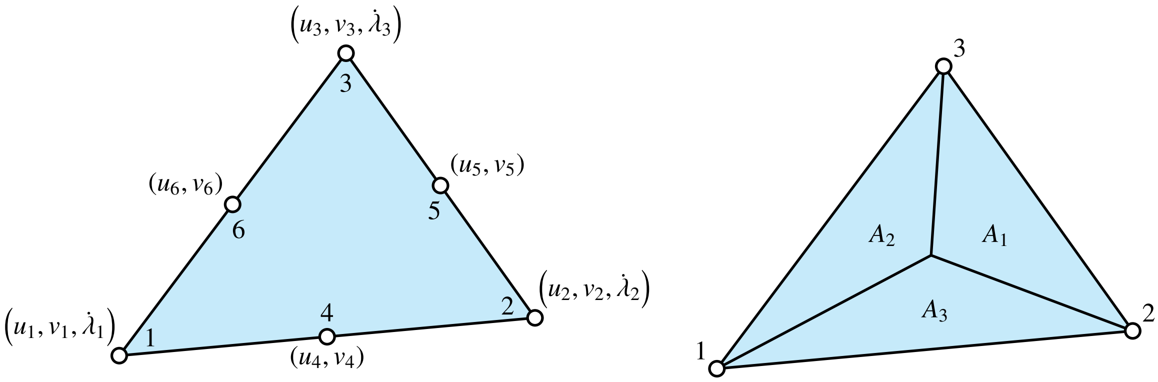

(a) Six-node triangular element

(b) Area coordinates of the triangular element

Figure 1: Refinement procedure of the UBFEM with proposed error indicator-based mesh adaptive refinement scheme

element using the values at three vertices can be written as:

$$\dot{\varepsilon}(\boldsymbol{x}) = \sum_{i=1}^{3} N_i(\boldsymbol{x})\,\dot{\varepsilon}_i, \quad \dot{\lambda}(\boldsymbol{x}) = \sum_{i=1}^{3} N_i(\boldsymbol{x})\,\dot{\lambda}_i \tag{2}$$

2.2. Fundamentals of kinematic upper bound limit analysis

According to the upper bound theorem, the upper-bound method requires that the velocity field within the main failure zone satisfies the associated flow rule and compatibility conditions. Within such a velocity field, an upper bound solution of the ultimate collapse load is therefore obtained by equating the power expended by the external load to the power dissipated internally by the plastic deformation, which can be written as:

$$D_p(\boldsymbol{u}) = \int_V d_p(\boldsymbol{u})\,\mathrm{d}V \le W_{ext}(\boldsymbol{u}) \tag{3}$$

where $d_p(\boldsymbol{u})$ is the function of plastic dissipation, and $D_p(\boldsymbol{u})$ can be written as:

$$D_p(\boldsymbol{u}) = \sum_{k=1}^{N_c} \int_A 2c\cos\phi\dot{\lambda}\mathrm{d}A = 2c\cos\phi \sum_{k=1}^{N_c} \frac{1}{3} A_k \left(\dot{\lambda}_{k,1} + \dot{\lambda}_{k,2} + \dot{\lambda}_{k,3}\right) \tag{4}$$

in which c and ϕ are the cohesion and friction angle of the soil, N_c is the total number of elements in the computational domain, A_k is the area of kth element, $\dot{\lambda}_{k,i}$ is the plastic multiplier rate for ith node of kth element. In Eq. (3), $W_{ext}(\boldsymbol{u})$ is the power expended by external loads (including surcharge loading and other fixed loading) and written as:

$$W_{ext}(\boldsymbol{u}) = \beta W_{ext}^{*}(\boldsymbol{u}) + W_{ext}^{0}(\boldsymbol{u}) \tag{5}$$

where β is the load factor, and $W_{ext}^{*}(\boldsymbol{u})$ and $W_{ext}^{0}(\boldsymbol{u})$ are the power expended by the surcharge and fixed loads, respectively. It should be mentioned that the effect of water seepage force, which viewed as a source term of body force, is considered in the current formulation. For a specific element, the power of the water seepage force can be written as:

$$\begin{aligned} W_{ext}^{0}(\boldsymbol{u}) &= -\int_V \gamma_w i \cos\theta u \mathrm{d}V - \int_V \gamma_w i \sin\theta v \mathrm{d}V \\ &= -\sum_{k=1}^{N_c} \left(\boldsymbol{f}_{k,x}^{\mathrm{T}} \boldsymbol{u} + \boldsymbol{f}_{k,y}^{\mathrm{T}} \boldsymbol{v} \right) \end{aligned} \tag{6}$$

where i is the hydraulic gradient, θ is the angle of hydraulic gradient with respect to the horizontal direction, $\boldsymbol{u} = \begin{bmatrix} u_1 & u_2 & u_3 \end{bmatrix}$ and $\boldsymbol{v} = \begin{bmatrix} v_1 & v_2 & v_3 \end{bmatrix}$ are nodal velocity vectors at three vertices along x and y directions, and $\boldsymbol{f}_{k,x}$ and $\boldsymbol{f}_{k,y}$ are the seepage force vectors at three vertices of element k corresponding to the x and y directions, respectively. The seepage force vectors can be written as:

$$\begin{aligned} \boldsymbol{f}_{k,x} &= -\frac{1}{3}\gamma_w i \cos\theta A_k \begin{bmatrix} 1 & 1 & 1 \end{bmatrix} \\ \boldsymbol{f}_{k,y} &= -\frac{1}{3}\gamma_w i \cos\theta A_k \begin{bmatrix} 1 & 1 & 1 \end{bmatrix} \end{aligned} \tag{7}$$

It should be pointed out that the definitions of variables i and θ are provided in Fig. 2, and the calculation of their values will be further elaborated in the subsequent section.

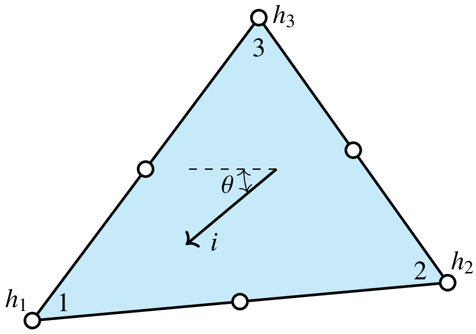

Figure 2: Schematic diagram of nodal water head and hydraulic gradient for the six-node triangular element

2.3. Seepage analysis in the upper bound limit analysis

2.3.1. Governing equations for the two-dimensional flow

For the effective stress analysis with the framework of upper bound method, the fundamental thing is to determine the seepage forces. To achieve this purpose, the distribution of total head in the ground is required to be known, which can be obtained by solving the groundwater flow equation. Under steady state flow condition, the two-dimensional flow can be defined by Laplace equation as follows:

$$k_x \frac{\partial^2 h}{\partial x^2} + k_y \frac{\partial^2 h}{\partial y^2} = 0 \tag{8}$$

where k_x and k_y are the soil permeabilities along the horizontal and vertical directions, respectively. In this study, it is assumed that the permeability is homogeneous in both directions, namely $k_x = k_y = k$, which gives:

$$\frac{\partial^2 h}{\partial x^2} + \frac{\partial^2 h}{\partial y^2} = 0 \tag{9}$$

with h being the total water head, which is the sum of water pressure head p/γ_w and elevation head Y (Sahoo and Kumar, 2019) and can be expressed as:

$$h = p/\gamma_w + Y \tag{10}$$

where p and γ_w are the pore water pressure and unit weight of water, respectively. Similar as the fields of plastic strain rate $\dot{\varepsilon}$ and plastic multiplier rate $\dot{\lambda}$, the variation in the total water head throughout each element can be written as:

$$h = \sum_{i=1}^{3} N_i h_i \tag{11}$$

where N_i and h_i are shape function and total water head at node i.

2.3.2. Seepage fields in the computational domain

Using Galerkin's method in combination with linear approximation, Eq. (9) can be rewritten as:

$$\iint [N]^{\mathrm{T}} \left(\frac{\partial^2 h}{\partial x^2} + \frac{\partial^2 h}{\partial y^2} \right) \mathrm{d}x\mathrm{d}y = 0 \tag{12}$$

Applying integration by parts, the above equation becomes:

$$\iint \left[\frac{\partial}{\partial x} \left([N]^{\mathrm{T}} \frac{\partial h}{\partial x} \right) + \frac{\partial}{\partial y} \left([N]^{\mathrm{T}} \frac{\partial h}{\partial y} \right) - \frac{\partial [N]^{\mathrm{T}}}{\partial x} \frac{\partial h}{\partial x} - \frac{\partial [N]^{\mathrm{T}}}{\partial y} \frac{\partial h}{\partial y} \right] \mathrm{d}x\mathrm{d}y = 0 \tag{13}$$

Following Stokes' theorem, the first two terms of Eq. (21) can be written as:

$$\iint \frac{\partial}{\partial x} \left([N]^{\mathrm{T}} \frac{\partial h}{\partial x} \right) \mathrm{d}x\mathrm{d}y = \oint [N]^{\mathrm{T}} \frac{\partial h}{\partial x} n_x \mathrm{d}s \tag{14}$$

$$\iint \frac{\partial}{\partial y} \left([N]^{\mathrm{T}} \frac{\partial h}{\partial y} \right) \mathrm{d}x\mathrm{d}y = \oint [N]^{\mathrm{T}} \frac{\partial h}{\partial y} n_y \mathrm{d}s \tag{15}$$

where n_x and n_y are the unit outward normal vector to any specific boundary surface ds. When substituting Eqs. (14) and (15) into Eq. (21), the following equation can be determined as:

$$\oint [N]^{\mathrm{T}} \frac{\partial h}{\partial x} n_x \mathrm{d}s + \oint [N]^{\mathrm{T}} \frac{\partial h}{\partial y} n_y \mathrm{d}s - \iint \frac{\partial [N]^{\mathrm{T}}}{\partial x} \frac{\partial h}{\partial x} \mathrm{d}x\mathrm{d}y - \iint \frac{\partial [N]^{\mathrm{T}}}{\partial y} \frac{\partial h}{\partial y} \mathrm{d}x\mathrm{d}y = 0 \tag{16}$$

Incorporating the variation in the total water head h throughout each element, the final discretised two-dimensional flow equation for a specific element within the problem domain can be defined as:

$$\underline{\oint [N]^{\mathrm{T}} \left(\frac{\partial h}{\partial x} n_x + \frac{\partial h}{\partial y} n_y \right) \mathrm{d}s} - \iint \frac{\partial [N]^{\mathrm{T}}}{\partial x} \frac{\partial [N]}{\partial x} \mathrm{d}x\mathrm{d}y \, \{h\} - \iint \frac{\partial [N]^{\mathrm{T}}}{\partial y} \frac{\partial [N]}{\partial y} \mathrm{d}x\mathrm{d}y \, \{h\} = 0 \tag{17}$$

It should be noted that the first term (underlined) in Eq. (19) becomes zero for internal elements, whereas for elements along the external boundary, it represents the flux of the total water head (if applicable). In matrix form, Eq. (19) can be rewritten as:

$$\mathbf{k}_e \boldsymbol{h}_e = \boldsymbol{X}_e \tag{18}$$

in which

$$\mathbf{k}_e = \frac{1}{4A}\begin{bmatrix} \eta_1^2+\xi_1^2 & \eta_1\eta_2+\xi_1\xi_2 & \eta_1\eta_3+\xi_1\xi_3 \\ \eta_1\eta_2+\xi_1\xi_2 & \eta_2^2+\xi_2^2 & \eta_2\eta_3+\xi_2\xi_3 \\ \eta_1\eta_3+\xi_1\xi_3 & \eta_2\eta_3+\xi_2\xi_3 & \eta_3^2+\xi_3^2 \end{bmatrix}, \quad \boldsymbol{h}_e = \begin{Bmatrix} h_1 \\ h_2 \\ h_3 \end{Bmatrix}, \quad \boldsymbol{X}_e = \begin{Bmatrix} X_1 \\ X_2 \\ X_3 \end{Bmatrix}$$

After assembling above elemental matrices given in Eq. (22) into a global matrix for all elements, the total water heads (h values) at each node of the seepage field can be obtained by imposing associated seepage boundary conditions. In this study, the distribution of total water head for the considered problem domain can be calculated through in-house finite element method code. Based on the solution of nodal total water heads, the hydraulic gradient (i) within each element and its direction can be determined using the principle of hydromechanics and geometric relationships and written as:

$$\begin{aligned} i_x^e &= \frac{h_1(y_3-y_2)+h_2(y_1-y_3)+h_3(y_2-y_1)}{x_1y_2+x_2y_3+x_3y_1-x_1y_3-x_2y_1-x_3y_2} \\ i_y^e &= -\frac{h_1(x_3-x_2)+h_2(x_1-x_3)+h_3(x_2-x_1)}{x_1y_2+x_2y_3+x_3y_1-x_1y_3-x_2y_1-x_3y_2} \\ \tan\theta &= -\frac{h_1(x_3-x_2)+h_2(x_1-x_3)+h_3(x_2-x_1)}{h_1(y_3-y_2)+h_2(y_1-y_3)+h_3(y_2-y_1)} \end{aligned} \tag{19}$$

where i_x^e and i_y^e are the hydraulic gradients for a specific finite element along the horizontal and vertical directions. The determined values of total water head (h) and hydraulic gradient (i) are thus used for calculating the seepage force, which has been discussed in the above section.

2.4. Formulation of second-order cone programming

In this study, we make an assumption that the soil follows the Mohr-Coulomb yield criterion. Under two-dimensional conditions, the criterion can be expressed as:

$$F = \left(\sigma_x-\sigma_y\right)^2 + \left(2\tau_{xy}\right)^2 - \left[2c\cos\phi - \left(\sigma_x+\sigma_y\right)\sin\phi\right]^2 \leq 0 \tag{20}$$

where σ_x and σ_y are the stress components along x and y directions, and τ_{xy} is the shear stress component. According to Makrodimopoulos and Martin (2007), Eq. (20) can be rewritten as:

$$F_k = A_k\sigma_x + B_k\sigma_y + C_k\tau_{xy} - 2c\cos\phi = 0 \tag{21}$$

where $A_k = \cos\alpha_k + \sin\phi$, $B_k = \sin\phi - \cos\alpha_k$, $C_k = \sin\alpha_k$, $\alpha_k = 2k\pi/p$, and p is the total number of sides of the circumscribed polygon. In a similar manner, after introducing auxiliary variables ρ_1 and ρ_2, the second-order conic form of the Mohr-Coulomb yield criterion can be expressed as:

$$\sqrt{\rho_1^2+\rho_2^2} \leq \dot{\lambda} \tag{22}$$

Referring to previous studies (Sloan, 1989; Sloan and Kleeman, 1995; Makrodimopoulos and Martin, 2007), a Second-Order Cone Programming (SOCP) model within the framework of the UB-RTME is constructed. This model aims to solve the objective function, which represents the optimal difference between the power expended by the external load and the power dissipated internally. The SOCP model can be expressed in matrix form as follows:

$$
\begin{aligned}
& \min\left(\int_V d_p\left(\boldsymbol{\varepsilon}\right) dV - W_{ext}^0\right) \\
& \boldsymbol{Bs} = 0 \\
& \boldsymbol{Cs} = \boldsymbol{b} \\
& \dot{\lambda} \geq \sqrt{\rho_1^2 + \rho_2^2} \\
& \boldsymbol{q}^T \boldsymbol{u} = 1
\end{aligned}
\tag{23}
$$

where $\boldsymbol{Bs} = 0$ represents the linear constraint condition, $\boldsymbol{s}$ corresponds to the optimization variable matrix for global linear constraint, which includes nodal velocity components (u_i and v_i), elemental plastic multipliers $\dot{\lambda}$, and auxiliary variables (ρ_1 and ρ_2), $\boldsymbol{Cs} = \boldsymbol{b}$ defines the velocity constraint condition, and $\boldsymbol{q}$ represents the nodal load matrix. In such a way, the final load factor β can be determined by solving the SOCP model. For a more comprehensive understanding, the readers are suggested to refer to the work of Sloan (1989), Sloan and Kleeman (1995), and Makrodimopoulos and Martin (2007), as well as our recent work (Zheng and Yang, 2022).

3. Adaptive refinement scheme

When performing an adaptive mesh refinement in the UBFEM, the fundamental thing is to determine which elements need to be refined. This section presents an novel adaptive refinement scheme with an error indicator for quantitatively evaluate the error in the nodal plastic energy dissipation of each element within the framework of UBFEM. The criterion for adaptivity activation and termination conditions of the proposed adaptive mesh refinement are addressed.

3.1. Adaptivity activation and termination conditions

It is known that the total number of adaptive steps and finite elements required to be refined in each step are generally controlled by the adaptive refinement scheme, which defines the remeshing criteria that governing the automatic adjustment of the mesh (more details can be found in Zheng and Yang (2022)). For a regular refinement scheme in the UBFEM, the plastic dissipation of each element is frequently adopted as an indicator for performing the refinement strategy (Dörfler, 1996; Martin, 2009; Nguyen-Xuan et al., 2016; Zhang et al., 2019b). In this manner, after sorting the values of plastic dissipation η_m for all elements in a decreasing order, the refinement criteria for determining the elements that need to be refined can be written as:

$$
\sum_{\Omega_r \subseteq \Omega} \eta_m \geq \theta_r \sum_{m=1}^{N_c} \eta_m \tag{24}
$$

where Ω_r is the group of elements that required to be refined, Ω is the group of all elements in the computational domain, θ_r is the refinement coefficient that controls the refinement extent, and N_c is the total number of elements in the computational domain. From Eq. (24), it can be concluded that the total number of refined elements continues to increase with an increase in the total number of elements in the problem domain, which sometimes leads to an excessive mesh refinement and a significant increased computational burden (Zheng and Yang, 2022).

As stated above, the refinement scheme proposed by Dezfooli et al. (2022, 2023) ensures that the rate new elements are added to the current mesh gradually decreases during the refinement process. For this reason, a similar refinement criterion is thus proposed and incorporated into the UBFEM. Following those proposed by Dezfooli et al. (2022, 2023), the average value of the nodal error in plastic dissipation energy is introduced and defined as E_{ave}, which is written as:

$$E_{ave} = \sum_{i=1}^{N_c} \frac{Err_i}{A_i} / \sum_{i=1}^{N_c} \frac{1}{A_i} \tag{25}$$

where Err_i is nodal error of plastic dissipation energy for ith element. In a similar manner, for each adaptive step, mesh refinement is activated when the value of E_{ave} is larger than a prescribed threshold (η_{cri}), while terminated when the value of E_{ave} becomes smaller than the value of η_{cri}. Apart from this termination condition, the adaptive procedure is also considered to terminate when the difference between the upper bound solution of the last refinement step and that from one step before becomes smaller than a predefined values δ_{cri}, which is written as:

$$\frac{|\beta^n - \beta^{n-1}|}{|\beta^{n-1}|} \leq \delta_{\text{cri}} \tag{26}$$

where β_n and β_{n-1} are the obtained upper bound solutions for the last refinement step and one step before, respectively. In this study, the predefined values of η_{cri} and δ_{cri} are chosen as 1.0×10^{-4} and 5.0×10^{-5}, respectively. It should be mentioned that smaller values of η_{cri} and δ_{cri} can be beneficial for generating more accurate upper bound solutions, and as a result it can lead to a significant increase in the computational cost.

3.2. Error indicator in kinematic upper bound finite element method

In the context of the UBFEM, it has been observed that the solution error tends to be more pronounced in the local regions where the plastic multiplier rates are higher. This behavior is quite similar to what is observed in the traditional FEM. For quantitatively assessment, a simple error indicator based on the evaluation of the difference in nodal plastic dissipation energy is proposed within the framework of the UBFEM. To accomplish this, the difference in the nodal plastic multiplier rates for an arbitrary element i with three local nodes can be expressed as:

$$\Delta\dot{\lambda}_i^{(m,n)} = \dot{\lambda}_i^{(m)} - \dot{\lambda}_i^{(n)}; \quad (m,n) \in \{(1,2)\,;(2,3)\,;(1,3)\} \tag{27}$$

where $\dot{\lambda}_i^{(m)}$ is the plastic multiplier rate for node m of element i. Referring to the definition proposed in Dezfooli et al. (2022, 2023), the error indicator for ith element is thus defined as:

$$Err_i = \max\left(\left(\frac{2}{3} c \cos\phi A_i \Delta\dot{\lambda}_i^{(m,n)}\right)^2\right); \quad (m,n) \in \{(1,2)\,;(2,3)\,;(1,3)\} \tag{28}$$

which defines the maximum nodal difference in the plastic dissipation energy for ith element. It should be noted that, for the cohesionless soil, the error indicator given in Eq. (28) is no longer applicable as the values of Err_i become zero.

In this study, a very small value of cohesion, namely $c = 0.001$ kPa (solely adopted for the purpose of determining the error indicator), has been adopted in order to mitigate numerical issue as well as improve the computational efficiency.

3.3. Refinement criteria and procedure

For the adaptive refinement scheme, another significant part is to determine those elements that are most suitable to be refined, which must be specified in the refinement criteria. Following Dezfooli et al. (2022, 2023), the refinement criterion adopted in this study is expressed as:

$$Err_i \geq \ln\left(\max\left(\alpha_c N_c, 1.01\right)\right) \times \ln\left(\max\left(\alpha_n N_n, 1.01\right)\right) \times E_{ave} \tag{29}$$

where α_c and α_n are two predefined parameters that control the level of adaptive refinement. Unlike previous adopted mesh refinement scheme, this refinement criteria ensures that the total number of refined elements gradually decreases with adaptive step. After determining those most suitable refined elements, the adaptive refinement is thus performed by longest edge bisection of those triangular elements. Details regarding the refinement procedure of the UBFEM with proposed error indicator-based mesh adaptive refinement scheme proposed in the current work are summarized in Fig. 3.

4. Numerical verification and application

4.1. Homogeneous slope subjected to pore water pressure

For the validation of the UBFEM with the proposed error indicator-based mesh refinement scheme, the stability of soil slopes subjected to pore water pressure is investigated in this section, which was previously studied by Chen et al. (2004) and Kim et al. (1999). As shown in Fig. 4, this study addresses the stability of a two-dimensional soil slope subjected to pore water pressure. The slope with an inclination of $\alpha = 45°$ is assumed to rest upon an impervious and rigid base with a depth of $H = 10.0$ m and a depth ratio of $D = 2.0$. The effective cohesion c', effective friction angle ϕ', and permeability k of the soil are assumed to be homogeneous and isotropic across the entire slope. For validation purposes, the soil properties are considered to be $\gamma = 18.0\,\mathrm{kN/m^3}$, $c' = 20.0\,\mathrm{kN/m^2}$, and $\phi' = 15°$. To address the influence of the pore water pressure, six distinct locations of the water table (H_w) above toe level are considered. These levels span from 0 to $1.0H$ at intervals of $0.2H$. For each defined slope configuration, a similar unstructured initial mesh is utilized in the analysis. The boundaries at the base are assumed to be non-slip and impermeable, while free-slip conditions are enforced with a constant water head (partly enforced on the right hand side of the problem domain based on the value of H_w/H) at two-lateral boundaries.

To evaluate the computational efficacy of the UBFEM in conjunction with the proposed error indicator-based mesh refinement scheme, Table 1 compares the upper bound solution of the load factor β obtained from the present study and Optum G2 for slopes under varying water table locations with $\alpha_c = 0.005$ and $\alpha_n = 0.005$. For further comparative insight, the final total number of elements (N_e) are also included. From the results, it can be seen that

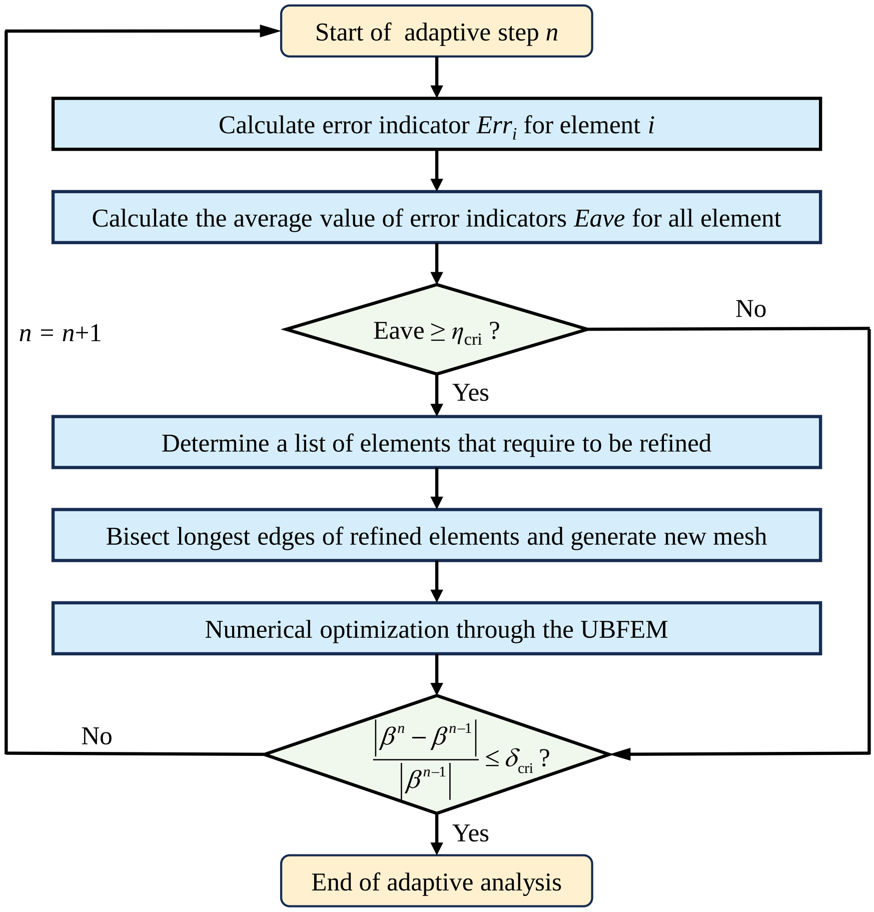

Figure 3: Refinement procedure of the UBFEM with proposed error indicator-based mesh adaptive refinement scheme

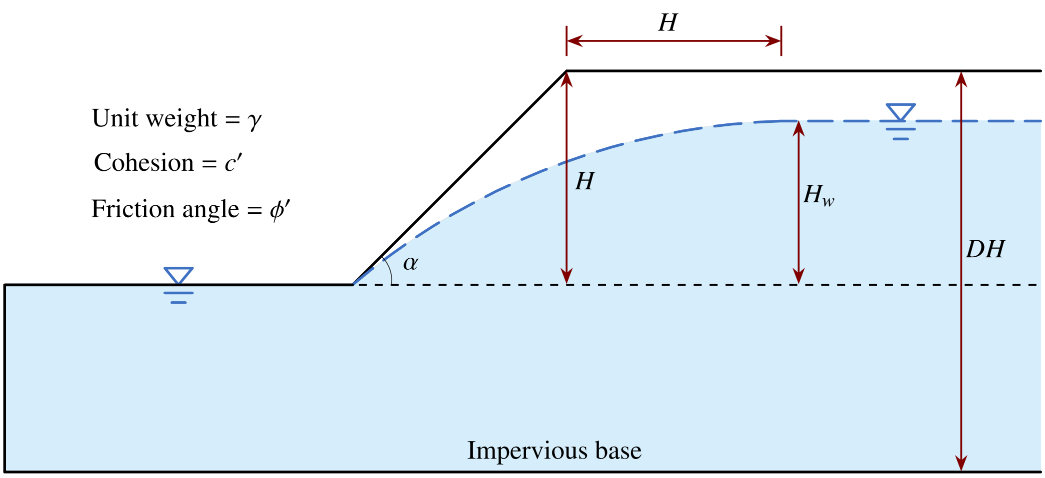

Figure 4: Problem geometry for the soil slope subjected to the pore water pressure

the proposed upper bound solutions match quite well with the upper bound solutions of Optum G2 for all considered cases. The maximum relative error with respective to the solution of Optum G2 is less than 1%. In addition, more rigorous upper bound solutions are deduced for the proposed method even with a small amount of total number of elements N_e (generally less than 60% of the later). This comparison confirms the exceptional efficacy of integrating the error indicator-based mesh refinement scheme into the UBFEM.

Table 1: Comparison of load factors β and number of elements N_e for slopes with different values of H_w/H obtained from present study and Optum G2.

H_w/H	Present study (UB)		Optum G2 (UB)		Relative error e_r [%]
	β	N_e	β	N_e	
0	1.330	6688	1.332	11169	0.04
0.2	1.314	5848	1.325	11161	0.82
0.4	1.265	6464	1.273	11290	0.89
0.6	1.218	4102	1.228	11422	0.90
0.8	1.203	5886	1.204	11554	0.14

As discussed in the above section, two predefined parameters, α_c and α_n, have been incorporated into the refinement criterion of Eq. (29) to control the level of mesh refinement in the adaptive analyses. To study the influence of mesh refinement control parameters, Table 2 gives the comparison of adaptive analyses for a slope with $H_w/H = 0.6$ using 7 different combinations of α_c and α_n with an initial total number of elements $N_e = 424$. For comparison, the resulting CPU times are normalised with respect to the computational cost in the scenario where $\alpha_c = 0.001$ and $\alpha_n = 0.005$, while the relative errors of load factors are computed in relation to the corresponding value of β for the same case (analysis II). As expected, a more stringent upper bound load factor β can be deduced with increasing values of α_c and α_n. Nonetheless, this comes at the expense of substantially heightened computational time, primarily due to the pronounced increase in the total number of elements. In addition, it can be seen that further reducing both the values of α_c and α_n beyond the analysis II leads to a slight improvement in solution accuracy but significantly reduces computational efficiency. For instance, when comparing the analyses I and II, it can be concluded that the normalized CPU time increases by a factor of 5.79 when α_n decreases from 0.005 to 0.001. This comparison emphasizes the significance of a proper chosen of mesh refinement control parameters in adaptive analyses to strike a balance between solution accuracy and computational cost.

For further illustration, Fig. 5 presents the final adaptive meshes for a homogeneous slope in the presence of seepage forces under various combinations of mesh refinement control parameters (α_c and α_n) obtained from the UBFEM with the proposed mesh refinement scheme. Notably, mesh refinement primarily concentrates in the vicinity of the shear band, which can readily capture the potential failure mechanisms of slopes under the influence of groundwater seepage flow, especially for the cases shown in Figs. 5(a) and 5(b). Moreover, it can be observed that highly localised refined meshes are obtained with $\alpha_c = 0.001$ and $\alpha_n = 0.005$. In contrast, the localised refined band becomes slightly

Table 2: Comparison of adaptive analyses for a slope with $H_w/H = 0.6$ and initial $N_e = 424$ under varying values of α_c and α_n

Analysis ID	α_c	α_n	β	N_e	Normalised CPU time	Relative error [%]
I	0.001	0.001	1.212	16906	5.790	-0.351
*II	0.001	0.005	1.216	5515	1.000	0.00
III	0.005	0.005	1.218	4102	0.869	0.164
IV	0.005	0.01	1.219	3511	0.773	0.265
V	0.01	0.01	1.220	2816	0.617	0.341
VI	0.02	0.01	1.224	2187	0.579	0.622
VII	0.1	0.1	1.256	681	0.192	3.295

* Reference for normalisations and error calculations

narrower than that of $\alpha_c = 0.001$ and $\alpha_n = 0.001$ owing to a significant increase in the total number of elements. For this reason, in this example, it is recommended to select mesh refinement control parameters as $\alpha_c = 0.001$ and $\alpha_n = 0.005$. However, it should be mentioned that the selection of α_c and α_n is problem dependent and will be further explored in the following examples.

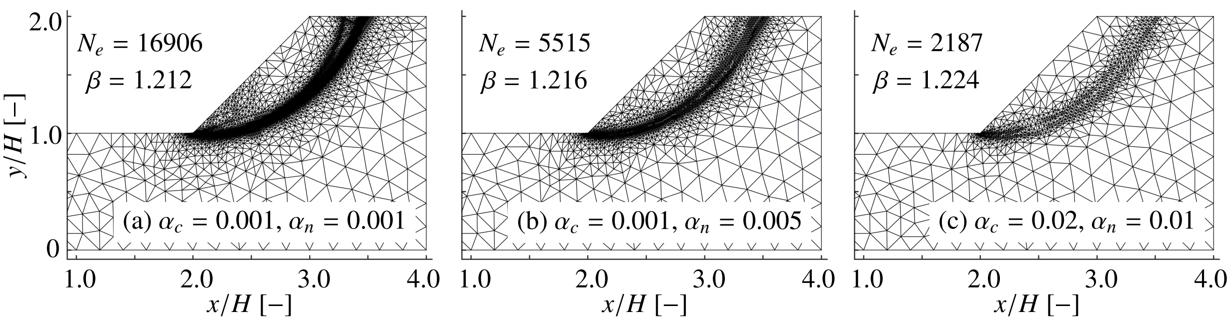

Figure 5: Final adaptive meshes for a homogeneous slope with $H_w/H = 0.6$ under various combinations of α_c and α_n

It should be mentioned that the stability of the slope is generally assessed by calculating the factor of safety (F), which defines the ratio of shear strength parameters (c' and ϕ') that need to be reduced in order to bring the slope to a limit state of equilibrium (Chen et al., 2004). Following this definition, the reduced shear strength parameters c'_e and ϕ'_e are thus written as:

$$c'_e = c'/F \tag{30a}$$

$$\tan\phi'_e = \tan\phi'/F \tag{30b}$$

Table 3 compares the factors of safety F for homogeneous slopes obtained from Kim et al. (1999), Chen et al. (2004), and the proposed method. Note that, for the solutions of Chen et al. (2004), only those obtained using finer meshes are included. From Table 3, it can be noticed that the proposed upper bound solutions locate between the upper and lower bound solutions of Kim et al. (1999), and they also match quite well with the upper bound solutions of Chen et al. (2004) with finer meshes. With H_w/H varying from 0.2 to 0.6, the maximum difference between the proposed solutions and those average values of upper and lower bound solutions from Kim et al. (1999) is less than 4.0%. These comparisons further verify the effectiveness of the proposed mesh refinement scheme in combination with the UBFEM.

Table 3: Comparison of the factors of safety F for homogeneous slopes with different values of H_w/H.

H_w/H	Present study	Kim et al. (1999)		Chen et al. (2004)	Relative error e_r [%][b]
	Upper bound	Upper bound	Lower bound	Upper bound[a]	
0.2	1.169	1.230	1.101	–	0.30
0.4	1.139	1.166	1.036	1.202	3.45
0.6	1.060	1.068	0.971	1.096	3.97

[a] Only these solutions obtained using finer meshes are included;

[b] Defines the difference between the proposed solutions and those average values of upper and lower bound solutions from Kim et al. (1999).

Apart from upper bound solutions, as an example, Fig 6 shows the adaptive meshes for slopes with $H_w/H = 0.6$ at four different levels of refinement stages obtained from the UBFEM with the proposed error-based mesh refinement scheme. It can be seen that, mesh refinement primarily concentrates at some local area, which can vividly reproduce the major slip surface and the potential failure mechanism of slopes, with an increased refinement iterations. In addition, the upper bound solution of load factor β is found to converge to a constant value with an increased total number of elements. This observation can also be noticed from the solutions of Optum G2 and the UBFEM with regular mesh refinement schemes, which are omitted for the purpose of simplicity.

4.2. Stability of a circular tunnel under steady state seepage condition

In this section, the two-dimensional stability of a circular tunnel under a steady state seepage condition is studied (Sahoo and Kumar, 2019). As shown in Fig. 7, the circular tunnel has a diameter of D and burial depth H. The elevation of groundwater table above the tunnel crown is assumed to be H_w, while the thickness of the dry soil layer above the groundwater table is defined as H_d. The dry and submerged unit weights of the soil are respective defined as γ_d and γ', while soil friction angles below and above ground water table are considered to be ϕ and ϕ', respectively. Consistent with the definitions proposed by Sahoo and Kumar (2019), it is assumed that the soil friction angles below and above ground water table are identical, namely $\phi = \phi'$. Similarly, the boundaries are assumed to be non-slip and impermeable for the base. Free-slip conditions are enforced with a constant water head (partly enforced on the right hand side of domain according to the value of H_w) at two-lateral boundaries, while a zero water pressure head is considered along the circumference of the circular tunnel. No surface surcharge loads are applied, so that the collapse process is exclusively driven by the gravity loading. Therefore, it is quite important to determine the ultimate support pressure σ_s that required to maintain the stability of the circular tunnel driven under the groundwater table.

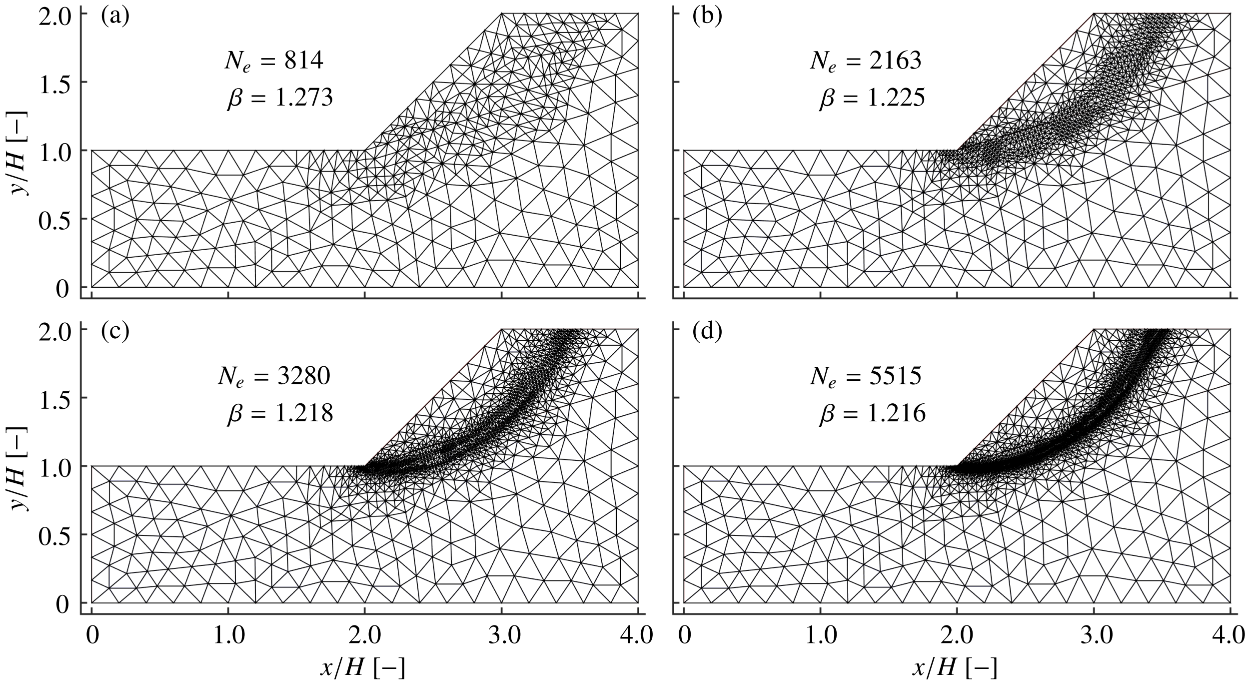

Figure 6: Adaptive meshes for homogeneous slopes with $H_w/H = 0.6$ at different levels of refinements obtained by the UBFEM in combination with the proposed error indicator-based mesh refinement scheme.

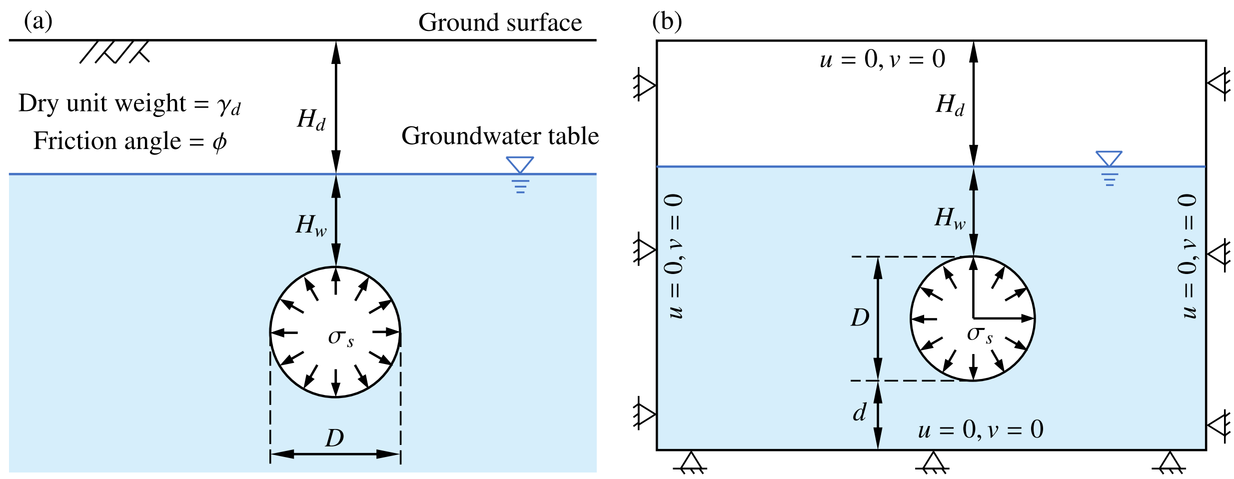

Figure 7: Stability of a circular tunnel under steady state seepage condition: (a) definition of problem, and (b) chosen domain and boundary condition.

In accordance with the research conducted by Sahoo and Kumar (2019), the ultimate support pressure that required to maintain the stability of the tunnel driven under the groundwater table is defined in a dimensionless form as $\sigma_s/(\gamma' D)$. In this specific scenario, it is considered that the dimensionless support pressure $\sigma_s/(\gamma' D)$ mainly depends on the soil friction angle ϕ, the elevation of groundwater table above the tunnel crown H_w, the thickness of dry soil layer H_d, and soil unit weight above and below the groundwater table. For the purpose of comparative illustration, the groundwater table is considered to locate at the ground surface in this study,which gives $H_d = 0$. Two different ratio between the unit weight of the water and the unit weight of the submerged soil, including $\gamma_w/\gamma' = 0.8$ and 1.5, are thus considered.

Fig. 8 provides a comparative analysis of the ultimate support pressures $\sigma_s/(\gamma' D)$ derived from the present study and those from Sahoo and Kumar (2019) for circular tunnels with varying dimensionless burial depth H/D. It should be mentioned that for both cases the groundwater table is is precisely positioned at the ground surface. In Fig. 8, it can be concluded that the proposed upper bound solutions of $\sigma_s/(\gamma' D)$ match quite well with those lower bound solutions proved by Sahoo and Kumar (2019). As expected, a slightly lower magnitude of $\sigma_s/(\gamma' D)$ is required to maintain the stability of the tunnel from the upper bound method, highlighting the robustness of the proposed upper bound solution. In addition, the magnitude of $\sigma_s/(\gamma' D)$ is found to decrease with an increase in the soil friction angle, while it becomes larger with an increased burial depth H/D and a decreased ratio of γ_w/γ'. These observations are in consistent with the conclusions drawn by Sahoo and Kumar (2019).

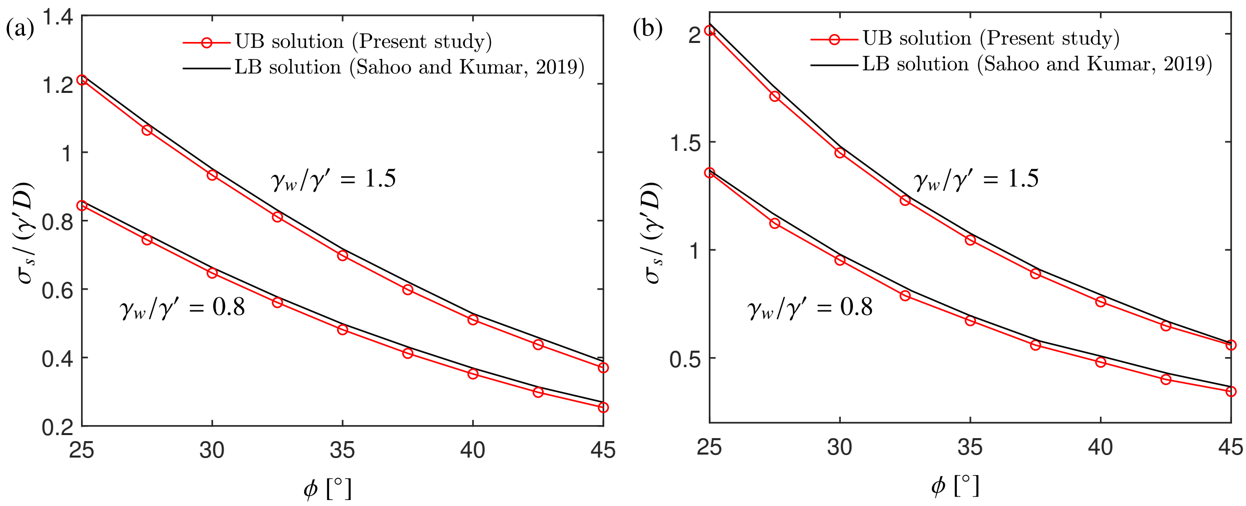

Figure 8: Comparison of $\sigma_s/(\gamma' D)$ obtained from present study and those from Sahoo and Kumar (2019) for circular tunnels with: (a) $H/D = 1$ and $H_w/D = 1$, and (b) $H/D = 3$ and $H_w/D = 3$.

As an example, Fig. 9 displays the adaptive meshes for a circular tunnel under different adaptive iterations for the case of $\phi = 25°$, $\gamma_w/\gamma' = 0.8$, $H/D = 3$, and $H_w/D = 3$. Using the UBFEM in combination with the proposed error indicator-based h-adaptive refinement scheme, as shown in Figs. 9(a)-9(b), highly localised mesh refinement primarily concentrates in the vicinity of the shear zone and the shear bands lightly narrows with an increase in the adaptive iteration. This highly localised mesh refinement area can vividly capture the potential failure pattern of the circular tunnel with the presence of pore water pressure, which confirms the excellent performance of the proposed method in reproducing the potential failure mechanism.

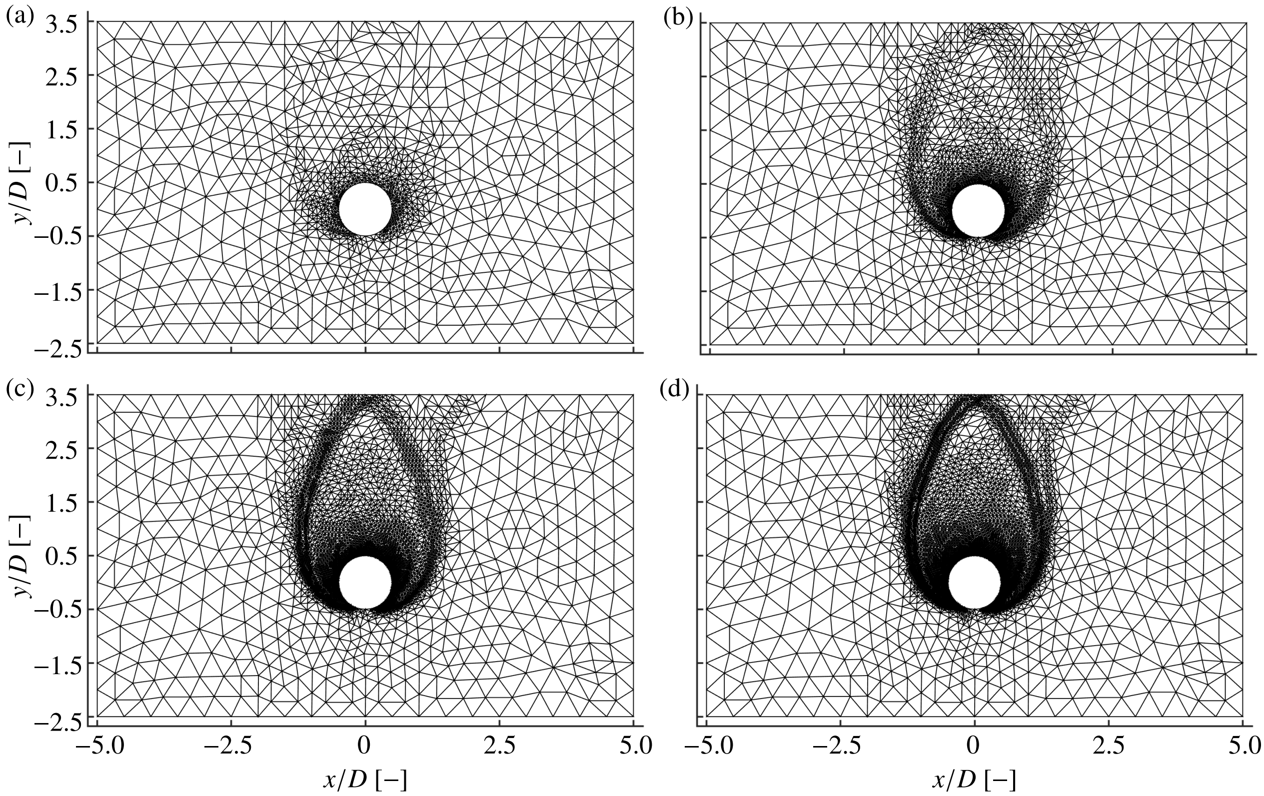

Figure 9: Adaptive meshes for a circular tunnel under steady state seepage condition for the case of $\phi = 25°$, $\gamma_w/\gamma' = 0.8$, $H/D = 3$, and $H_w/D = 3$.

5. Conclusions

In the present study, a simple, yet efficient, error indicator-based h-adaptive refinement scheme in kinematic upper-bound limit analysis with the presence of seepage forces is presented. The proposed method is established using six-node quadratic triangular elements and a Second-Order Cone Programming (SOCP). An novel adaptive refinement scheme with an error indicator for quantitatively evaluate the error in the nodal plastic energy dissipation of each element within the framework of UBFEM is thus provided,and the criterion for adaptivity activation and termination conditions of the proposed adaptive mesh refinement are also addressed. Moreover, in a similar manner as treating the unit weight of the soil, the effects of seepage forces are incorporated as body forces in the upper bound formulation. Numerical procedure of the proposed error indicator-based h-adaptive refinement scheme incorporating with the inclusion of seepage forces are given and implemented in the in-house code. Two benchmark problems are numerically analyzed to evaluate the excellent performance of the error indicator-based h-adaptive refinement scheme in kinematic upper-bound limit analysis with the presence of seepage forces. Numerical solutions and comparisons support the conclusion that the proposed method can provide more accurate and efficient upper bound solutions with a significant smaller amount of elements. Further extension of the proposed refinement scheme to 3D upper bound limit analysis will be carried in our future work.

CRediT authorship contribution statement

Xiangcou Zheng: Conceptualization, Methodology, Software, Validation, Investigation, Funding acquisition, Writing – original draft. **Feng Yang**: Conceptualization, Methodology, Writing – review & editing. **Shuying Wang**: Conceptualization, Writing – review & editing. **Junsheng Yang**: Conceptualization, Writing – review & editing. **Ashraf Osman**: Conceptualization, Methodology, Writing – review & editing.

Declaration of Competing Interest

The authors declare that they have no known competing financial interests or personal relationships that could have appeared to influence the work reported in this paper.

Acknowledgements

This work was supported by the National Natural Science Foundation of China (No. 52308425), the International Postdoctoral Exchange Fellowship Program-Talent-Introduction Program (No. YJ20220219), and China Postdoctoral Science Foundation (No. 2023TQ0382).

Data availability statement

The data that support the findings of this study are available from the corresponding author upon reasonable request.

References

Andersen, K.D., Christiansen, E., Conn, A.R., Overton, M.L., 2000. An efficient primal-dual interior-point method for minimizing a sum of euclidean norms. SIAM Journal on Scientific Computing 22, 243–262.

Andersen, K.D., Christiansen, E., Overton, M.L., 1998. Computing limit loads by minimizing a sum of norms. SIAM Journal on Scientific Computing 19, 1046–1062.

Borges, L., Zouain, N., Costa, C., Feijóo, R., 2001. An adaptive approach to limit analysis. International Journal of Solids and Structures 38, 1707–1720.

Chen, J., Yin, J.H., Lee, C., 2004. Rigid finite element method for upper bound limit analysis of soil slopes subjected to pore water pressure. Journal of engineering mechanics 130, 886–893.

Ciria, H., Peraire, J., Bonet, J., 2008. Mesh adaptive computation of upper and lower bounds in limit analysis. International journal for numerical methods in engineering 75, 899–944.

Dezfooli, M.S., Khoshghalb, A., Shafee, A., 2022. An automatic adaptive edge-based smoothed point interpolation method for coupled flow-deformation analysis of saturated porous media. Computers and Geotechnics 145, 104672.

Dezfooli, M.S., Khoshghalb, A., Shafee, A., Khalili, N., 2023. An h-adaptive edge-based smoothed point interpolation method for elasto-plastic analysis of saturated porous media. Computers and Geotechnics 162, 105628.

Di, Q., Li, P., Zhang, M., Wu, J., 2023. Influence of permeability anisotropy of seepage flow on the tunnel face stability. Underground Space 8, 1–14.

Di, Q., Li, P., Zhang, M., Zhang, W., Wang, X., 2022. Analysis of face stability for tunnels under seepage flow in the saturated ground. Ocean Engineering 266, 112674.

Dörfler, W., 1996. A convergent adaptive algorithm for poisson's equation. SIAM Journal on Numerical Analysis 33, 1106–1124.

Graine, N., Hjiaj, M., Krabbenhoft, K., 2021. 3d failure envelope of a rigid pile embedded in a cohesive soil using finite element limit analysis. International Journal for Numerical and Analytical Methods in Geomechanics 45, 265–290.

Keawsawasvong, S., Ukritchon, B., 2019. Undrained basal stability of braced circular excavations in non-homogeneous clays with linear increase of strength with depth. Computers and Geotechnics 115, 103180.

Keawsawasvong, S., Ukritchon, B., 2021. Undrained stability of plane strain active trapdoors in anisotropic and non-homogeneous clays. Tunnelling and Underground Space Technology 107, 103628.

Keawsawasvong, S., Ukritchon, B., 2022. Design equation for stability of a circular tunnel in anisotropic and heterogeneous clay. Underground Space 7, 76–93.

Kim, J., Salgado, R., Yu, H., 1999. Limit analysis of soil slopes subjected to pore-water pressures. Journal of Geotechnical and Geoenvironmental Engineering 125, 49–58.

Krabbenhoft, K., Damkilde, L., 2003. A general non-linear optimization algorithm for lower bound limit analysis. International Journal for Numerical Methods in Engineering 56, 165–184.

Krabbenhøft, K., Lyamin, A., Sloan, S., 2007. Formulation and solution of some plasticity problems as conic programs. International Journal of Solids and Structures 44, 1533–1549.

Krabbenhoft, K., Lyamin, A.V., Hjiaj, M., Sloan, S.W., 2005. A new discontinuous upper bound limit analysis formulation. International Journal for Numerical Methods in Engineering 63, 1069–1088.

Le, C.V., 2013. A stabilized discrete shear gap finite element for adaptive limit analysis of mindlin–reissner plates. International Journal for Numerical Methods in Engineering 96, 231–246.

Lim, K., Li, A.J., Schmid, A., Lyamin, A., 2017. Slope-stability assessments using finite-element limit-analysis methods. International Journal of Geomechanics 17, 06016017.

Lyamin, A.V., Sloan, S., 2002. Upper bound limit analysis using linear finite elements and non-linear programming. International Journal for Numerical and Analytical Methods in Geomechanics 26, 181–216.

Makrodimopoulos, A., Martin, C., 2007. Upper bound limit analysis using simplex strain elements and second-order cone programming. International journal for numerical and analytical methods in geomechanics 31, 835–865.

Martin, C., 2009. Undrained collapse of a shallow plane-strain trapdoor. Géotechnique 59, 855–863.

Martin, C., 2011. The use of adaptive finite-element limit analysis to reveal slip-line fields. Géotechnique Letters 1, 23–29.

Munoz, J., Bonet, J., Huerta, A., Peraire, J., 2009. Upper and lower bounds in limit analysis: adaptive meshing strategies and discontinuous loading. International Journal for Numerical Methods in Engineering 77, 471–501.

Nguyen-Xuan, H., Wu, C., Liu, G., 2016. An adaptive selective es-fem for plastic collapse analysis. European Journal of Mechanics-A/Solids 58, 278–290.

Pastor, J., Thai, T.H., Francescato, P., 2003. Interior point optimization and limit analysis: an application. Communications in Numerical Methods in Engineering 19, 779–785.

Qian, Z., Li, A., Merifield, R., Lyamin, A., 2015. Slope stability charts for two-layered purely cohesive soils based on finite-element limit analysis methods. International Journal of Geomechanics 15, 06014022.

Sahoo, J.P., Kumar, B., 2019. Support pressure for stability of circular tunnels driven in granular soil under water table. Computers and Geotechnics 109, 58–68.

Sloan, S., 1988. Lower bound limit analysis using finite elements and linear programming. International Journal for Numerical and Analytical Methods in Geomechanics 12, 61–77.

Sloan, S., 1989. Upper bound limit analysis using finite elements and linear programming. International Journal for Numerical and Analytical Methods in Geomechanics 13, 263–282.

Sloan, S., 2013. Geotechnical stability analysis. Géotechnique 63, 531–571.

Sloan, S., Kleeman, P., 1995. Upper bound limit analysis using discontinuous velocity fields. Computer methods in applied mechanics and engineering 127, 293–314.

Tin-Loi, F., Ngo, N., 2003. Performance of the p-version finite element method for limit analysis. International Journal of Mechanical Sciences 45, 1149–1166.

Ukritchon, B., Keawsawasvong, S., 2018. Three-dimensional lower bound finite element limit analysis of hoek-brown material using semidefinite programming. Computers and Geotechnics 104, 248–270.

Ukritchon, B., Keawsawasvong, S., 2019. Three-dimensional lower bound finite element limit analysis of an anisotropic undrained strength criterion using second-order cone programming. Computers and Geotechnics 106, 327–344.

Ukritchon, B., Keawsawasvong, S., 2020a. Undrained lower bound solutions for end bearing capacity of shallow circular piles in non-homogeneous and anisotropic clays. International Journal for Numerical and Analytical Methods in Geomechanics 44, 596–632.

Ukritchon, B., Keawsawasvong, S., 2020b. Undrained stability of unlined square tunnels in clays with linearly increasing anisotropic shear strength. Geotechnical and Geological Engineering 38, 897–915.

Ukritchon, B., Yoang, S., Keawsawasvong, S., 2020. Undrained stability of unsupported rectangular excavations in non-homogeneous clays. Computers and Geotechnics 117, 103281.

Wang, S.T., Yang, X.L., Huang, F., Pan, Q.J., 2021. Three-dimensional upper-bound analysis of rock slopes subjected to seepage forces based on hoek-brown failure criterion. Computers and Geotechnics 138, 104310.

Xiao, Y., Zhao, M., Zhao, H., Zhang, R., 2018. Finite element limit analysis of the bearing capacity of strip footing on a rock mass with voids. International Journal of Geomechanics 18, 04018108.

Yang, F., Zheng, X., Zhang, J., Yang, J., 2017. Upper bound analysis of stability of dual circular tunnels subjected to surcharge loading in cohesive-frictional soils. Tunnelling and Underground Space Technology 61, 150–160.

Yang, F., Zheng, X.C., Zhao, L.H., Tan, Y.G., 2016. Ultimate bearing capacity of a strip footing placed on sand with a rigid basement. Computers and Geotechnics 77, 115–119.

Zhang, J., Ding, L., Liang, Y., Zong, J., Li, Z., 2019a. Upper-bound finite element adaptive analysis of plane strain heading in soil with a soft upper layer and hard lower layer. Advances in Civil Engineering 2019.

Zhang, R., Chen, G., Zou, J., Zhao, L., Jiang, C., 2019b. Study on roof collapse of deep circular cavities in jointed rock masses using adaptive finite element limit analysis. Computers and Geotechnics 111, 42–55.

Zhang, R., Li, L., Zhao, L., Tang, G., 2018. An adaptive remeshing procedure for discontinuous finite element limit analysis. International Journal for Numerical Methods in Engineering 116, 287–307.

Zheng, X., Yang, F., 2022. An efficient and synchronous mesh refining–coarsening strategy in kinematic upper-bound limit analysis. Computers and Geotechnics 148, 104843.